JOURNAL OF MATERIALS SCIENCE **39** (2004) 3659– 3676

The role of structure on the thermal properties of graphitic foams

J. W. KLETT, A. D. MCMILLAN, N. C. GALLEGO, C. A. WALLS
Metals and Ceramics Division, Oak Ridge National Laboratory, Oak Ridge, TN 37831, USA
E-mail: klettjw@ornl.gov

A high conductivity graphite foam developed at Oak Ridge National Laboratory (ORNL) owes its unique thermal properties to the highly aligned graphitic structure along the cell walls. The material exhibits a peak in thermal conductivity at temperatures similar to that of highly ordered natural graphite, indicating the foam has an extremely graphitic nature. This paper explores the graphitic structure of the foam and attempts to correlate the morphology of the ligaments with the bulk thermal properties, up to 182 W/m·K. First, the manufacturing process of the foam and the resulting material properties are reported. Then, several models for representing the bulk materials properties are reviewed. Examination by optical image analysis, scanning electron microscopy (SEM) and transmission electron microscopy (TEM) was used to examine the structure of the graphite foam. In addition, crystallographic structure determined by X-ray diffraction is reported. A simple two parameter model of the morphology was developed and then used to predict the overall thermal properties of the foam based on the assumed highly ordered ligament structure. This new model correlated (within 5%) thermal conductivity to density of several foams, provided the average ligament conductivity could be accurately represented. From the new model and the material characterization data, it was determined that the average ligament thermal conductivity of the foam is $>$1650 W/m·K at room temperature, and increases to more than 2300 W/m·K at liquid nitrogen temperatures.

1. Introduction

Carbon foams were first developed by researchers in the late 60's as a reticulated vitreous (glassy) carbon foam. Ford [1] reported on carbon foams produced by carbonizing thermosetting organic polymer foams through a simple heat treatment. Then, Googin *et al.* [2] at the Oak Ridge Atomic Energy Commission Laboratory reported the first process dedicated to controlling the structure and material properties of carbon and graphitic foams by varying the precursor material (partially cured urethane polymer). In the several decades following these initial discoveries, many researchers explored a variety of applications for these materials [3–12] ranging from electrodes to insulating liners for temperatures up to 2500°C. In fact, reticulated carbon foams have been used as the template for many of the metal and ceramic foams currently used in industry. In the 1970's, research focused primarily on producing carbon foams from alternative precursors. For example, Klett [6] (no relation to this author) at the Sandia National Laboratories produced the first carbon foams from cork, a natural cellular precursor. Others worked on various processing and precursor changes in an attempt to modify properties and reduce cost. The majority of these carbon foams were used for thermal insulation, although some structural applications were found.

In the early 1990's, researchers at the Wright Patterson Air Force Base Materials Lab pioneered mesophase-derived graphitic foams, specifically for replacing expensive 3-D woven fiber performs in polymer composites and as replacements for honeycomb materials [13–20]. Their work was centered on developing a highly structural material that was lightweight, and to date, exhibits the highest specific strength of carbon foams. Concurrently, Ultramet Corp, performed research on RVC foam and used chemical vapor deposition (CVD) as a technique to place pyrolytic graphite on the glassy carbon ligaments of RVC, producing 3-D carbon structures with high-modulus ligaments.

With the goal of producing very inexpensive carbon foams, researchers at West Virginia University developed a method that used coal as a precursor for high strength foams with excellent thermal insulation properties [21–24]. In 1997, Klett [25–35] at the Oak Ridge National Laboratory (ORNL) reported the first graphitic foams with bulk thermal conductivities greater than 40 W/m·K (recently, conductivities up to 180 W/m·K have been measured [36]). By combining an open cellular structure with a thermal conductivity to weight ratio (κ/ρ) of greater than 200 (compared to 45 for copper), this material presents a unique opportunity to radically change the approach to solving many heat transfer problems. This graphite material has been

examined for the core of heat transfer devices such as radiators and heat sinks, evaporative cooling and phase change devices. Furthermore, the ability of the graphite foam to intercalate lithium and absorb acoustic energy makes them candidates for several applications beyond thermal management.

2. Experimental

2.1. Production method

The ORNL process for the manufacture of graphite foam is simple and free of oxidative stabilization traditionally required for processing of pitches and mesophases [19, 20, 37, 38]. First, a mesophase pitch precursor is heated, in a oxygen-free environment to about 50°C above its softening point.

Once the pitch has melted, the furnace pressure is elevated and the temperature raised at a controlled rate. While the pitch is molten, it begins to evolve low molecular weight species. These volatile gases form bubbles at nucleation sites on the bottom and sides of the crucible and rise to the top, beginning to orient the mesophase crystals in the vertical direction. With time, a significant amount of the mesophase crystals are oriented vertically.

At high temperatures the mesophase begins to pyrolyze (polymerize) and create additional volatile species. This pyrolysis weight loss, which can be very rapid and is dependent on the precursor, is accompanied by an increase in the molecular weight of the precursor which, in turn, increases the melt viscosity of the liquid mesophase. As the rapid evolution of gases progresses, the increase in viscosity tends to capture the bubbles in place, forcing the material to foam in the unrestrained direction, denoted as the *z*-direction. As the temperature of the furnace is further increased, the foamed mesophase continues to pyrolyze, further increasing the viscosity of the material until it has sufficiently cross linked and is rendered infusible (cannot be melted).

A typical resultant mesophase foam is illustrated in Fig. 1. The foam typically exhibits uniformly shaped bubbles with a normal distribution. The average pore size, orientation, and distribution is determined primarily by the pitch viscosity and processing pressure during foaming. Additionally, the mesophase foam will have a preferred orientation of crystals in the *z*-direction with an accompanying anisotropy of properties in the *z*-direction compared to those in the *x*-*y* plane even though the visual physical structure (bubble shape) may not be anisotropic.

While the foam synthesis process is rather simple, the morphological changes occurring during processing are rather complex. There is a delicate relationship between the viscosity-temperature behavior, melting temperature, and pyrolysis temperature of the mesophase pitch. Initially the pyrolysis gases develop at a temperature such that the viscosity is sufficient to result in a stable foam. Premature pyrolysis gas evolution causes the pitch to froth (like boiling milk) resulting in foam with a significant density gradient (this may be desirable in some applications). However, if the gases are evolved too late when the pitch viscosity is high, the bubbles may not be uniform, and cracking can occur due to thermal stresses. If the pyrolysis gases are evolved very slowly, as for certain high melting point Conoco pitches, the pores will tend to be smaller [39] overall.

Bubble formation is closely related to the autoclave operating pressure as well as temperature. Typically, the higher the autoclave gas pressure, the higher the temperature that gas evolution occurs, and the smaller the resulting pores. However, depending on the unique rheological properties of the starting pitch, the cell walls have different thicknesses, the bubble sizes can be dramatically different, and the mechanical and thermal properties can be affected. Unlike some other foaming techniques, such as slurry derived metallic foams, the resultant properties of the graphitic foam, (such as bubble size, ligament size, relative density, thermal and mechanical properties) are not independent properties. They are all dependent on the starting precursor's melt viscosity, pyrolysis temperature, and other pitch rheological properties.

The foamed mesophase is carbonized by heating to between 600 and 1000°C to yield a relatively pure carbon foam. In this state, the foam is an excellent thermal insulator with a bulk thermal conductivity of about 1.2 W/m·K for a foam with a density of 0.5 g/cm^3. Because the carbonized foam was formed with a mesophase that was not oxidatively stabilized

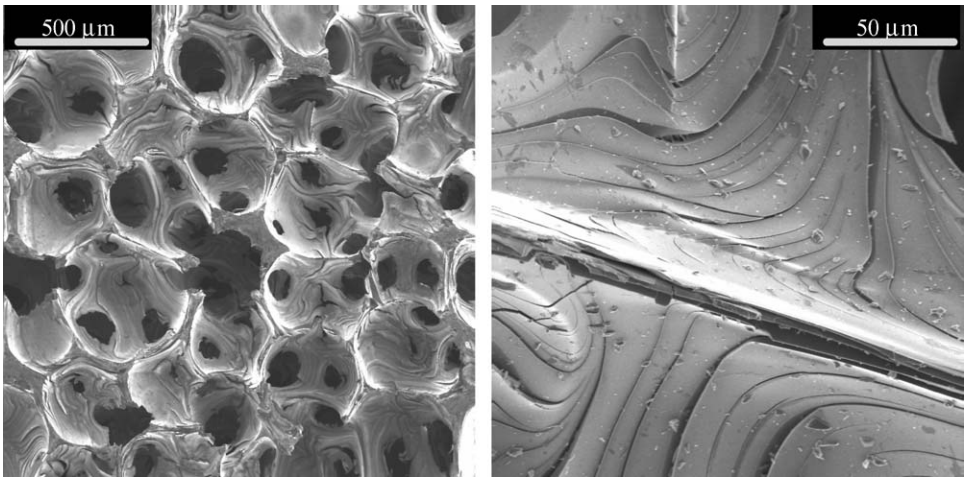

Figure 1 SEM images of mesophase pitch-derived foams.

during the pyrolysis/carbonization stages, the mesophase crystals are not inhibited and can grow to very large sizes. Consequently, when the carbon foam is converted to a highly graphitic foam by heat treatment to more than 2800°C under an argon purge, the resultant graphite crystals are highly aligned and significantly larger than those found in mesophase derived carbon fibers. Hence, the ligaments of the graphite foam produced with this method are more thermally conductive than even the best mesophase pitch-based graphite fibers.

Currently, the graphite foam manufacturing process has been licensed to Viatherm, Inc. and Poco Graphite, Inc. (manufactured as PocoFoam™ - www.pocofoam.com).

Using the process described above, several billets of foam (15 cm × 10 cm × 2.5 cm) were produced from Mitsubishi AR mesophase pitch powder with a softening point of 235°C. The pitch was foamed at 1000 psi pressure in aluminum pans utilizing a heating rate during foaming of 3.5°C/min [27]. The foaming consisted of heating under vacuum to 250°C, soaking for 1 h under vacuum, applying the foaming pressure, and then heating at the specified heating rate to 600°C, soaking for one hour, and then cooling to room temperature (while simultaneously reducing pressure) at approximately 1.25°C/min. All billets were then carbonized under an atmospheric nitrogen purge at a heating rate of 0.2°C/min to 1000°C. The billets were then cut into 0.625 cm cubes in a regular pattern throughout the foam billets and the Euclidian density was measured for each cube by mensuration.

2.2. Materials characterization

2.2.1. Density

Samples were machined into 1.65 cm cubes, cleaned ultrasonically with ethanol, dried and measured according to ASTM C559.

2.2.2. Scanning electron microscopy

A Hitachi S4700 Field Emission SEM at an accelerating voltage of 5 kV and an emission current of 15 μA was used to examine the foams at high magnifications. The samples used for density measurement were attached to the mounting fixture with electrically conductive carbon tape. Due to the high electrical conductivity of the graphite foams, samples were not gold sputter coated.

2.2.3. Thermal conductivity

The thermal diffusivity was determined using the thermal flash technique [40, 41] at room temperature on the same cubes used for density and SEM using a xenon flash lamp source. The diffusivity was measured on all three Cartesian planes, x, y, and z (with z being the foaming direction). The thermal conductivity was calculated from the following equation

$$\kappa = \alpha \cdot \rho \cdot C_{\mathrm{p}}$$

where, κ = Thermal conductivity (W/m·K), α = Thermal diffusivity (m^2/s), C_{p} = Specific heat (J/kg·K), and ρ = Density (kg/m^3).

The required values of the specific heat, C_{p}, are calculated from the following equation (taken from ASTM C781 [42]) which is valid from 300 to 3000 K.

$$C_{\mathrm{p}} = 8.426 \times 10^{-18}\,\mathrm{T}^6 - 4.300 \times 10^{-14}\,\mathrm{T}^5 - 1.245 \times 10^{-10}\,\mathrm{T}^4 + 1.353 \times 10^{-06}\,\mathrm{T}^3 - 3.765 \times 10^{-03}\,\mathrm{T}^2 + 4.796\mathrm{T} - 428.1$$

This equation reproduces the tabulated values within 0.1% for the indicated range of temperatures.

2.2.4. Optical image analysis

One method for characterizing graphitic structures is optical microscopy under cross-polarized light with a first-order-red wavelength retarder. This method can give basic understanding of a graphitic structure, although not detailed structure knowledge. With a wavelength retarder, graphitic planes oriented parallel to the axis of the retarder plate are highlighted blue while planes oriented perpendicular to the retarder plate are highlighted yellow. Planes that do not fall in either orientation, which include isotropic carbon as well as graphite in the 0, or 90 degree orientation, will be highlighted magenta. Therefore the sample is viewed as it rotates through 90 degrees to examine all regions to see if they shift from yellow to blue. Any magenta region that shifts to yellow or blue is graphitic and any magenta region that does not shift is most likely isotropic carbon.

For optical image analysis, foams were mounted in 1.25″ diameter mounting cups using Araldite GY 502 (Vantico Inc. North America) resin and Hysol HD 3416 hardener (Loctite Corporation) with a 10:1 (epoxy:hardener) ratio. Specimens were prepared by first grinding with 500, 800, 1200, and 2400 grit SiC grinding paper (30 N force at 150 rpm for 1 min each). Specimens were then polished with a Struers Polishing Machine (RotoForce 4 head/Rotopol 25 base) with DP-Purple Lubricant on 3 micron and 1 micron cloths (30 N force at 150 rpm for 10 min each).

A Nikon microphot microscope was used to examine the foams and a Polaroid PDMC3 color digital camera with 2.1 megapixil resolution was used to capture the images. The software package included with the camera (simple PCIp) was used for image enhancement. The first order red wavelength retarder plate was oriented in the −45 degree direction (90 degrees from typical microscopes), from the lower right to the upper left. Thus, graphitic planes oriented in the +45 degree orientation (perpendicular to the retarder plate) are highlighted yellow and those in the −45 degree orientation highlighted blue, as described above.

2.2.5. Transmission electron microscopy

When preparing the TEM specimens, it was found that the graphite foam was too soft for standard TEM sectioning. Therefore, the carbon foam was coated using chemical vapor infiltration with silicon carbide (SiC) [43], to deposit a layer of SiC approximately 20 microns thick on the surfaces throughout the cells of the

foam. The structural integrity of the SiC was sufficient to allow sectioning into standard TEM specimens. The final specimens were prepared by using focused ion beam milling (FIB) [44]. The specimens were analyzed on a Joel 4000EX TEM with an accelerating voltage of 400 kV.

2.2.6. X-ray diffraction

The crystallinity parameters, d_{002}, L_c, and L_a, were determined using these same samples on a Scintag PAD V vertical $\theta/2\theta$ goniometer. The diffractometer utilized Cu K_α radiation (45 kV and 40 mA) and a Si(Li) Peltier-cooled solid state detector. The data were collected as continuous scans, with a step size of $0.02^\circ 2\theta$ and a scan rate of $1^\circ 2\theta$/min between 10 and $90^\circ 2\theta$. Since a random orientation of the crystallites is already present in the foam, and since it was found that rotating the samples in the x, y, and z directions resulted in little change in the diffraction patterns, powdering was assumed to be unnecessary. This non-destructive technique on the foam allows the ability to perform different heat treatments on the same sample and measure the effects on the crystallite properties. The cubed samples were mounted directly in the X-ray beam and the diffraction patterns measured. Lattice spacing was determined from the indexed diffraction peak positions [45]. The 002 and 100 diffraction peak breadths were analyzed using the Scherrer equation to determine the crystallite dimensions in the -c and -a direction, respectively:

$$t = \frac{0.89\lambda}{B\cos(2\theta)},$$

where t is the average crystallite size in the sample, λ is the X-ray wavelength (1.540 Å), B is the breadth of the diffraction peak (full width half maximum (FWHM) minus the instrumental breadth, 0.06°), and 2θ is the diffraction angle.

3. Results and discussion

3.1. Thermal properties

Mesophase pitch-derived graphite foam made with the ORNL process will exhibit high bulk thermal conductivities, up to 182 W/m·K, at densities up to 0.6 g/cm^3 (see Table I). The foam conductivity is very dependent on the process used to make the foam, as discussed in the previous section.

Fig. 2 shows the effects of graphitization rate on the thermal conductivity for an ORNL graphitic foam made with process A. In all cases, the thermal conductivity in the z-direction is significantly higher than that in the x- or y-directions. The thermal conductivity in the x-y directions are relatively independent of the graphitization rate, while the thermal conductivity in the

TABLE I Properties of various graphite foams made with the ORNL method compared to commercially available PocoFoam™

	Foaming process	Graphitization rate (°C/min)	Average bulk density (g/cm^3)	Maximum deviation in density (%)	z-Plane thermal conductivity λ_z (W/m·K)	x-y Plane thermal conductivity λ_{xy} (W/m·K)
ORNL graphite foam	A	10	0.45	3.7	125	41
ORNL graphite foam	A	1	0.45	3.7	149	42
ORNL [35] graphite foam	B	10	0.59	–	150	–
ORNL graphite foam	B	1	0.59	–	181	60
PocoFoam™, billet 8001013	–	–	0.61	3.2	182	65

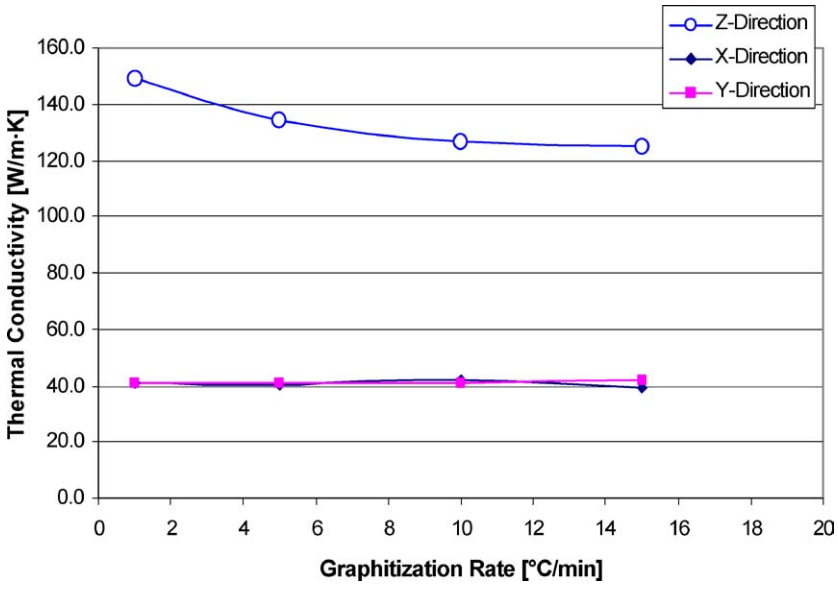

Figure 2 Effect of final heat treatment rate (graphitization) on the thermal properties of graphitic foams made with process A.

z-direction decreases with increasing graphitization rate. Kelly [46] reports that the strain energies during graphitization can be very high which ultimately will result in microcracks, lattice damage, and delamination of the graphite planes. Since the thermal properties in the axis of the graphite planes is many orders of magnitude greater than those normal to the planes, these graphitization stresses will tend to reduce the thermal properties in the direction parallel to the basal planes of the graphite, with little effect in the perpendicular planes where there is strain relief. With the knowledge that there is preferred orientation of the graphitic crystals in the z-direction, it is anticipated that heat treatment affects the z-direction conductivity with minimal impact in the x-y directions.

From Table I, it is apparent that the foaming process significantly influences the thermal conductivity through changes in density of the foam, while the final heat treatment rate affects the final thermal conductivity by affecting the structure of the ligaments.

3.2. Cryogenic thermal properties of graphite foam

One impressive characteristic of the graphitic foam is its thermal behavior at cryogenic temperatures. Typically, manufactured graphites exhibit a peak in thermal conductivity around room temperature [46–61]. As the order and perfection of the graphitic crystals improve and approach those of perfect graphite, this peak in conductivity shifts to lower temperatures around 80 K. Below this maximum temperature the thermal conductivity increases with temperature due to increasing specific heat. The decrease in thermal conductivity above the maximum temperature is caused by phonons scattering from intrinsic lattice defects and self scattering (Umklapp process). The exact location of the peak is largely controlled by the concentration of lattice defects. Defect free graphite such as the Canadian natural graphite [62] in Fig. 3 exhibit a peak at very low temperatures, whereas manufactured graphites typically exhibit a peak close to room temperature [61]. Significantly, the graphite foam data shows that the peak is below 100 K, which is characteristic of highly ordered graphites.

However, the conductivity shown in Fig. 3 for the foam is a bulk property instead of for the highly ordered foam ligaments. Thus, a useful comparison would be between the foam ligament thermal conductivities, $\lambda_{ligament}$, and Canadian Graphite. The need for estimates of ligament conductivity is therefore indicated.

3.3. Heat transport by phonons

Heat is transferred in the graphene lattice by vibrational modes represented as phonons. These vibrational modes are extremely complex [46–54, 63] but may be represented by the in-plane contributions and out-of-plane contributions. This heat transfer down the graphite lattice is extremely fast due to the very stiff nature of the covalent bonds. However, when a phonon reaches a defect in the structure, the vibration of the atoms is interrupted and the phonon is considered "scattered." In addition, the position and vibration of atoms in neighboring planes may impede the vibration of the atoms in the plane of interest.

The crystal perfection controls thermal conductivity. In addition, the crystal lattice must be oriented in such a manner that the vibration of atoms in neighboring planes does not interfere with the phonon transport in

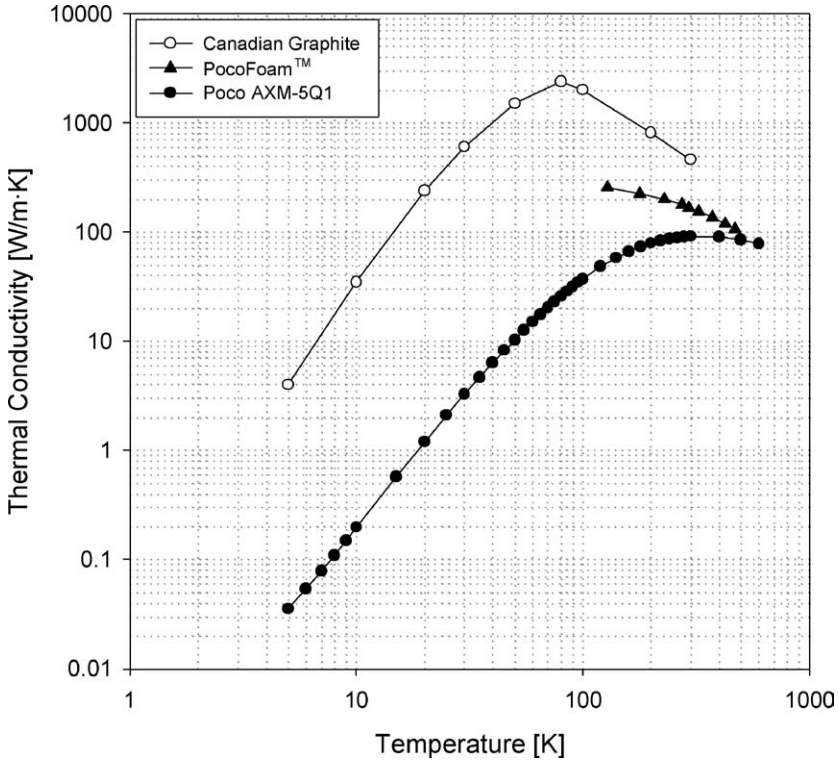

Figure 3 Thermal properties of PocoFoam™, Canadian Natural Graphite [62], and Poco AXM-5Q1 [61] versus temperature.

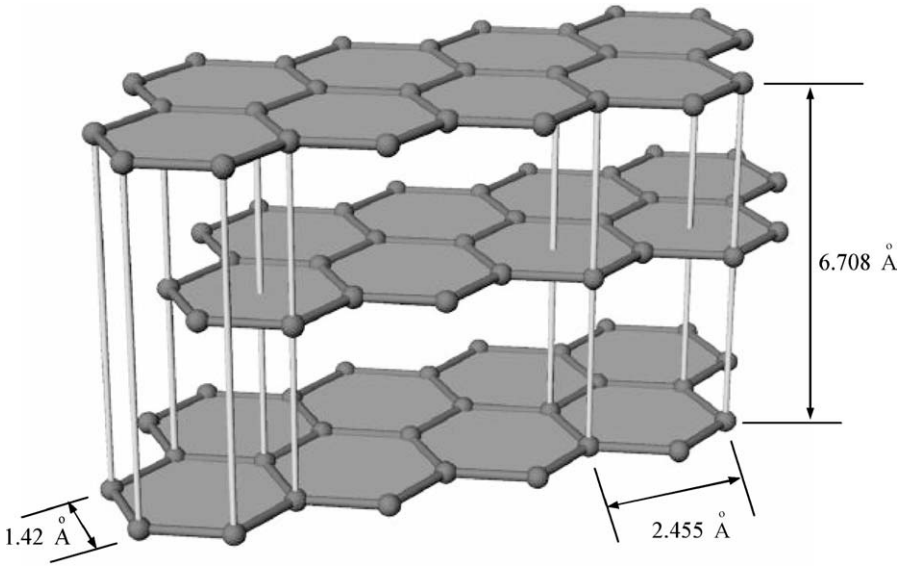

Figure 4 Planar structure of ABA stacking sequence of hexagonal graphite.

the plane of interest. This requires perfectly aligned, defect free graphene sheets wuth true 3D crystallinity. The hexagonal graphite structure requires an ABA stacking sequence shown in Fig. 4. In order to maintain the proper ABA stacking, the graphene sheets must be perfectly flat. If there is any curvature, the ABA stacking sequence will be disrupted over a given distance (depending on the radius of curvature), and the result will be scattering of phonons. As the radius of curvature decreases, there will be more scattering of phonons and decreased heat transfer. Furthermore, bending of a graphene plane is most likely due to defects (or vacancies) in the graphene lattice which force the structure to curve such as in fullerenes. Therefore, curvature of planes will result in scattering due to both out-of-plane contributions and in-plane contributions.

Even where the graphene lattice is perfect, it must be oriented in the appropriate direction (see Fig. 5). If there is any rotation of the planes, the atoms will not line up in the proper ABA stacking sequence, which will result

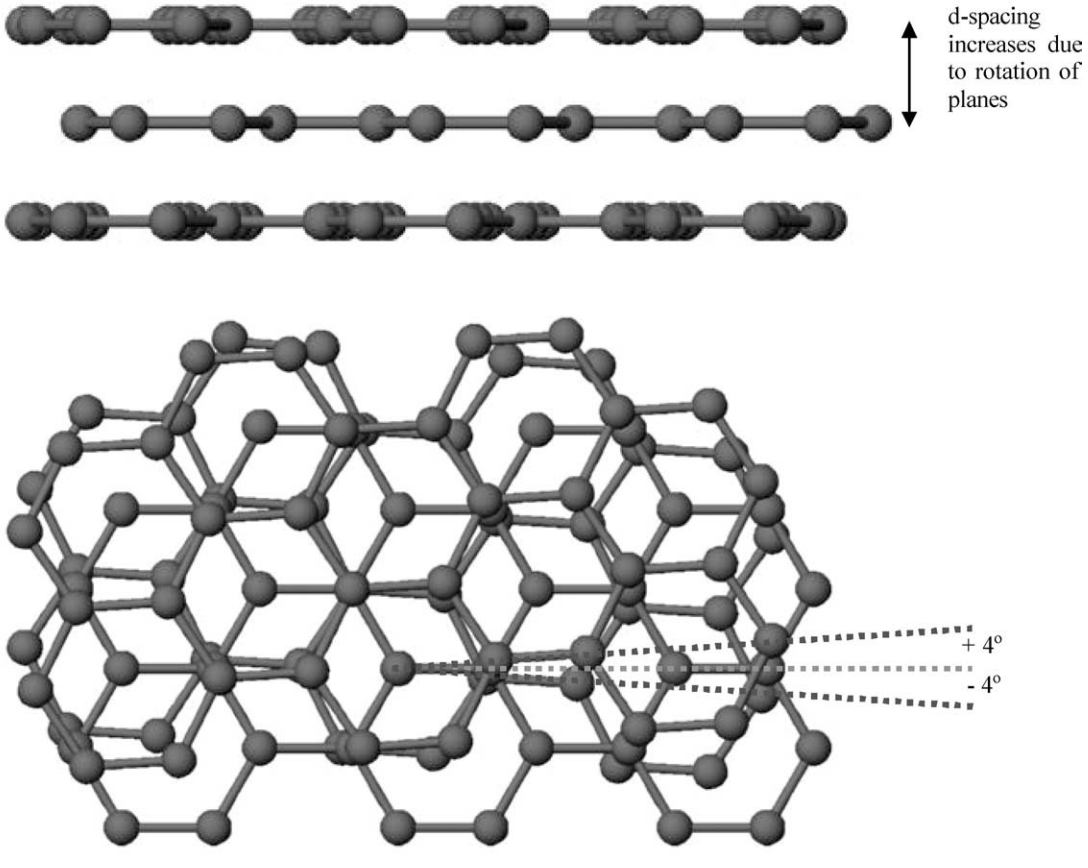

Figure 5 Graphite lattice which has flat planes with only 4° rotation of planes.

in a larger interplanar distance due to the interaction of Van der Walls forces and a decreased heat transfer through phonon scattering. A rotation of only 4 degrees can result in disruption of the lattice.

As discussed by Kelly [46–52] phonon transport is dominated by vibrational modes of the crystal lattice. Simply, the more perfect the lattice, the less the vibrations interact destructively to reduce heat transfer. However, there are many ways to disrupt and interfere with the phonon transfer. These include:

- Defects in the crystal lattice (vacancies, extra atoms, imperfect bonding, etc.)
- Folds in the graphite structure (lattice boundaries)
- Interlayer orientation and preferred orientation

The phonon mean free path is effectively the average distance along the graphene plane a phonon travels before it is scattered, either by a defect or by another phonon (destructive vibrational interference). Typically for most synthetic graphites, this length is small. However, in highly ordered graphites (like HOPG) the phonon mean free path can be quite large (on the order of 1000 nm).

To achieve high thermal conductivity in the graphite crystal, the structure must be comprised of aligned, straight graphene planes, resulting in the optimum in-plane and out-of-plane contributions to phonon transport. Moreover, the structure must have very large mean free paths for the phonons, requiring a relatively defect free structure to minimize phonon scattering along the plane. Any deviation from this simple model will decrease the phonon transport and the thermal conductivity.

Another mechanism relevant to the current work is Umklapp scattering, or phonon-phonon interactions. At low temperatures, such phonon self scattering is insignificant. However, as the temperature rises these interactions become more significant than lattice boundaries. For all graphites, the thermal conductivity decreases with increasing temperature above the maximum temperature.

3.4. Ligament properties

Table II compares the ligament and bulk thermal properties of several metal foams along with several ORNL graphite foams. Although copper and aluminum are conductive, reticulated foams made from these materials exhibit a relatively low bulk thermal conductivity. For example, copper has a ligament conductivity of 400 W/m·K but exhibits a thermal conductivity of only about 45 W/m·K at a relative density of 25%. Applying the same ratio to foams at a singular relative density suggests that the ORNL graphite foam ligament thermal conductivity, $\lambda_{ligament}$, is approximately 1200–1800 W/m·K.

TABLE II Thermal properties of various metal and graphite foams

	Relative density (%)	Ligament conductivity (W/m·K)	Measured bulk apparent conductivity (W/m·K)
Aluminum foam [64]	25	180	15
Copper foam [65]	10	400	15
Copper foam [64]	25	400	45
ORNL graphite foam[a]	26.5	?	150
ORNL graphite foam[b]	26.5	?	181

[a]Foaming rate B, graphitized at 10°C/min.
[b]Foaming rate B, graphitized at 1°C/min.

4. Physical characterization

From the discussion in Section 2.4, it is apparent that the crystallographic structure controls thermal conductivity. Here we present and discuss the results of detailed characterization of the microstructure of the foam.

4.1. Optical characterization

From optical image analysis using the first order red wavelength retarder, as shown in Fig. 6, the graphite foam is highly oriented. In fact, all regions shift from the yellow to blue upon stage rotation, indicating that they are graphitic structure. The ligaments appear to be more perfectly aligned than the junctions between them. The mesophase domains exhibit excellent flow texture within the ligaments, and the junctions exhibit more of a mosaic or random structure. Additionally, there is significant folding of the graphitic structure (sharp, crisp lines from yellow to blue). These fold regions could indicate boundaries of crystals with significant defects, or simply a large crystal with a "kink" in the graphite planes.

At higher magnifications (Fig. 7a), microcracks are revealed which predominantly follow the alignment of the crystals in the junctions running parallel to the graphite planes. Since the microcracks and crystals are fairly random in orientation, it would appear that they will inhibit heat transfer through this region of the foam, compared to that of the ligaments.

Fig. 7 shows the junctions of ORNL foams (process B foam graphitized at 10 and 1°C/min, along with that in a PocoFoam™ sample). It is clear from these images that the sample with the higher graphitization rate exhibits more significant microcracking in the junction, along with microcracks which traverse the heat conduction paths (perpendicular to the graphite planes). A slower heating rate allows the junctions to relieve stresses and reducing microcracks (with no apparent microcracks crossing the graphitic planes), resulting in higher thermal properties in this section. Additionally, there seems to be less folding of the graphitic structure. The ORNL samples seem to exhibit a fairly high content of disclinations in the junctions of the foams compared to that in the PocoFoam™. Few disclinations were observed in the ligaments of both PocoFoam™ and ORNL foam. Disclinations can serve as stress concentration points and initiate cracks [66]. Because of the disclinations, a more turbulent graphitic structure exists, thereby resulting in decreased heat transfer even though material may be highly graphitic.

The PocoFoam™ exhibited very few disclinations, resulting in a more aligned flow texture of the

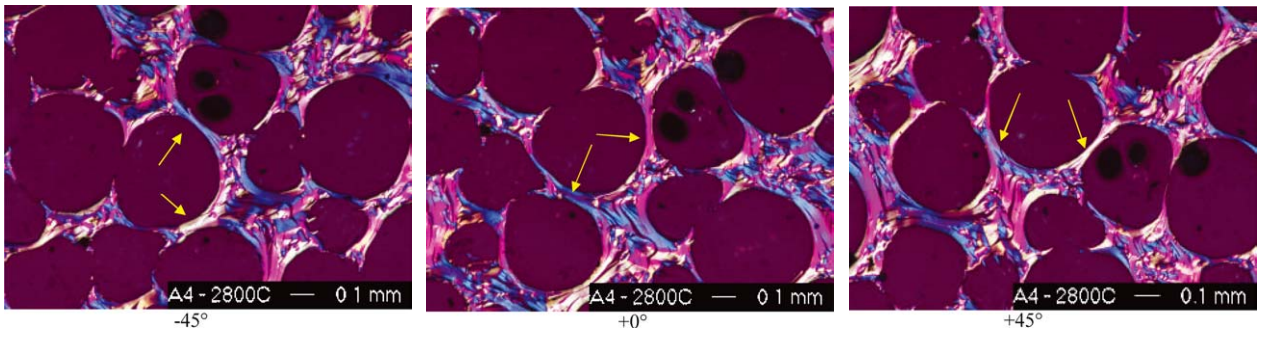

Figure 6 Optical micrographs of ORNL graphite foam graphitized at 10°C/min on a rotated stage illustrating highly ordered ligaments.

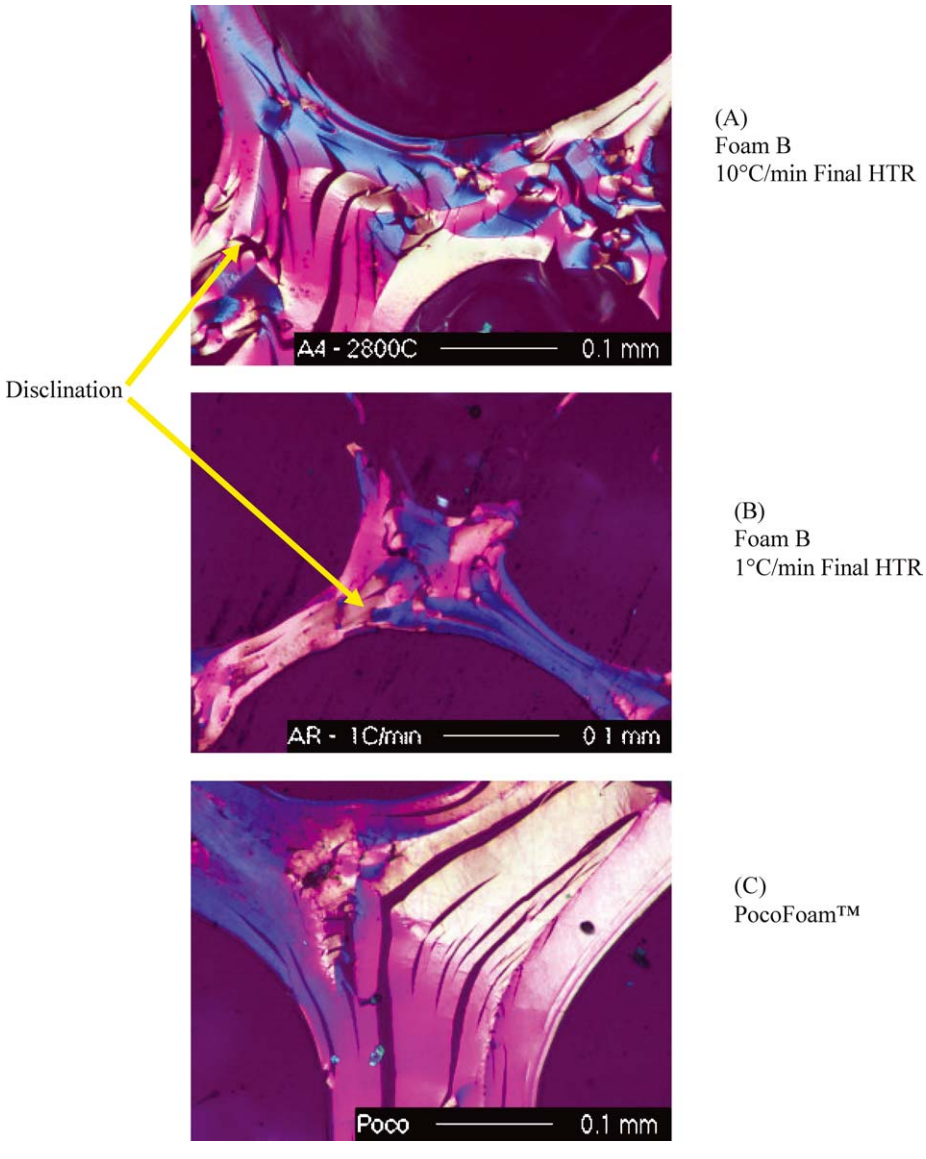

Figure 7 Optical micrographs of (a) ORNL graphite foam graphitized at 10°C/min, (b) ORNL foam graphitized at 1°C/min, and (c) PocoFoam^{TM}.

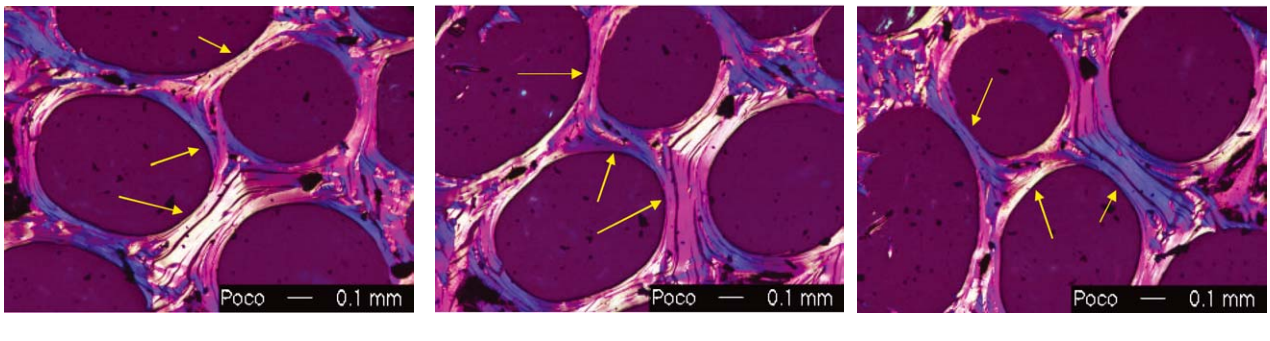

Figure 8 Optical micrographs of PocoFoam^{TM} illustrating high order in the junctions with significant porosity in the ligaments and junctions.

graphitic planes, enhancing heat transfer (Fig. 8). The PocoFoam™ exhibits a more desirable structure throughout the junction regions with little folding and all the microcracks running parallel to the graphitic planes. This, along with fewer disclinations in the ligaments, would lead to improved heat transfer in the PocoFoam™. However, more large pores are evident in ligaments of the PocoFoam™ compared to the ORNL foam. In addition, the final heat treatment rate of the PocoFoam™ is not reported and may be significantly different than that of the ORNL foams.

It is clear from the initial microscopy observations that the ligaments will be more conductive than the junctions because of folding, microcracking, and disclinations in the junction regions which inhibit heat transfer.

4.2. Scanning electron microscopy

The relative three dimensional structure of the graphite foams can be inferred by applying scanning electron microscopy. As seen in Fig. 9, the foam exhibits fairly uniform pore shapes, with a narrow pore size distribution (however quantitative data is best determined with optical image analysis). Also, virtually all cells are open and connected to several neighboring cells. Under higher magnification (Fig. 10), the ligaments (or cell walls) appear to contain highly aligned graphitic sheets oriented parallel to the ligament axis, confirming analysis with optical microscopy. The junctions appear to be graphitic, but exhibit a randomly oriented polycrystalline structure, as observed with optical microscopy.

At even higher magnification (Fig. 11), the fold structure within the junctions can be readily observed. One of these folds has apparently fractured, most likely due to residual stresses that form during heat treatment. The fold region does not resemble that found in polycrystalline graphite, but looks more like a continuous graphite flow domain with kinks in the structure. These folds will act as lattice boundaries and phonon scattering points, but are not as severe as a true crystal interface. Moreover, folds result in an increased heat flow path, further decreasing the overall heat flux.

The SEM images illustrate that the majority of microcracks run parallel to the graphene sheets. These cracks relieve thermal shrinkage stresses and impact the thermal properties less than transverse cracks. Curiously, there are several regions of highly aligned planes which appear to exhibit a sharp radius of curvature without any fractures or cracks (point A on Fig. 11). Such areas warrant further examination with TEM analysis.

4.3. Transmission electron microscopy

Transmission electron microscopy allows insight, at the atomic level, into many materials. However, it is extremely difficult to get good quality TEM images of highly graphitic materials because the microtoming techniques are difficult to apply on soft graphite structures. Hence, the samples of the graphite foam were first coated with silicon carbide to stiffen and rigidize the structure for the sample preparation procedure to yield reliable TEM images. The silicon carbide coating allowed for remarkable images to be obtained. Fig. 12 shows a foam ligament with its axis running from the lower left to the upper right. Clearly, the structure is highly aligned.

Several conclusions can be drawn from the image. First, the graphene planes are highly aligned and relatively defect free over extremely long ranges. There do not appear to be any bifurcations of the basal planes, which would result in large mean free paths. Moreover, there are several areas (one shown enlarged) where the

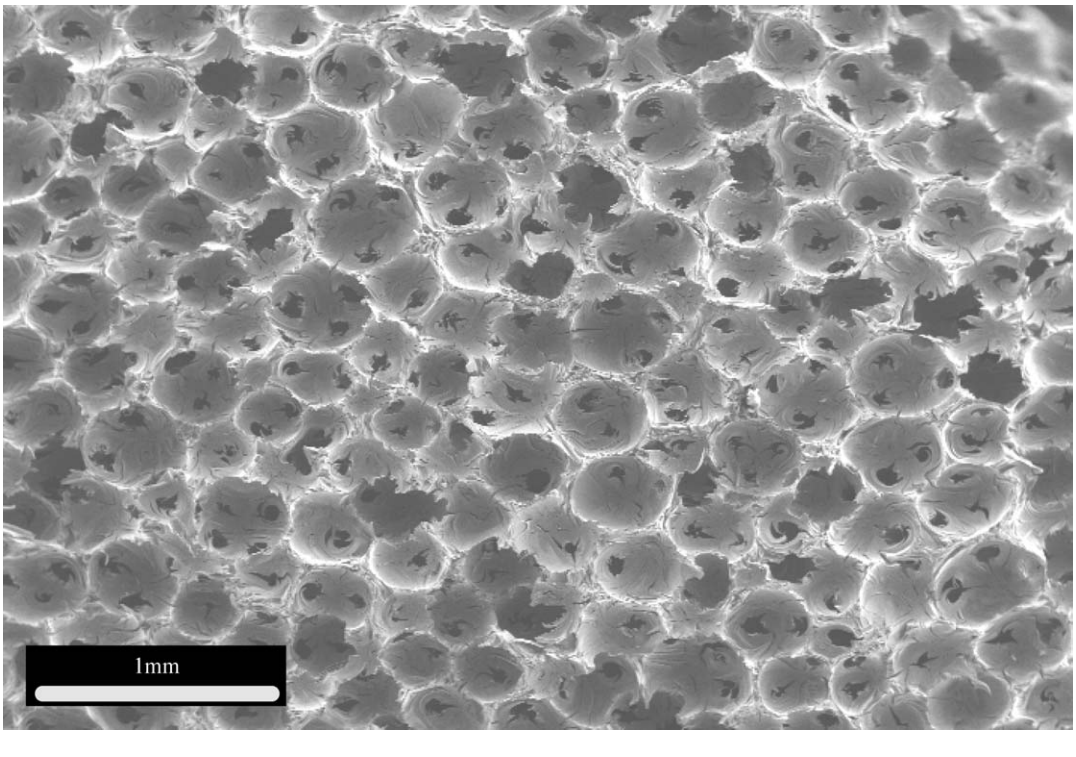

Figure 9 SEM of ORNL graphite foam B graphitized at 1°C/min.

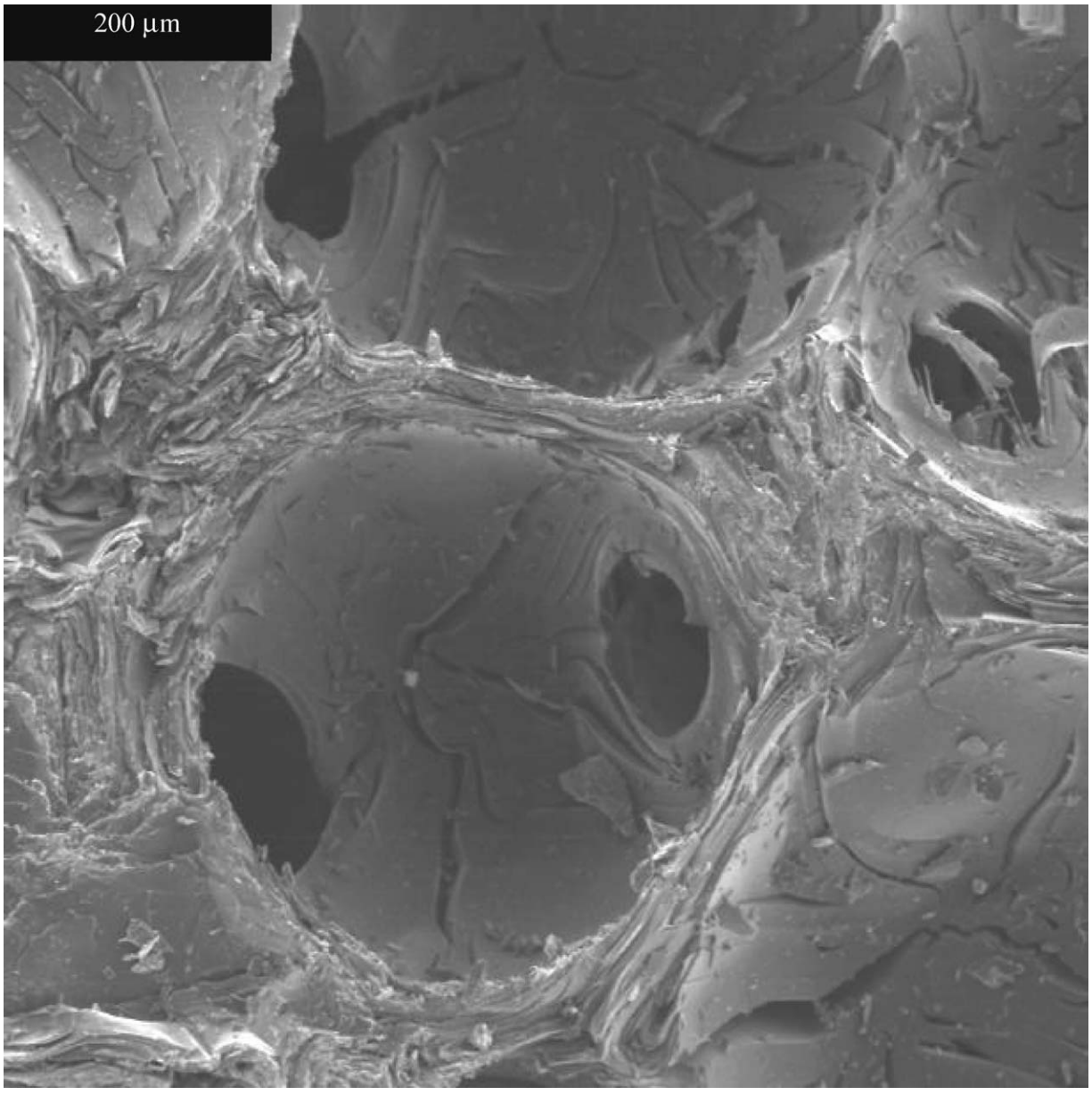

Figure 10 High magnification image of ORNL graphite foam B graphitized at 10°C/min illustrating highly aligned ligaments.

structure is aligned in true 3-D order such that both the 002 and the 110 planes are visible. The 002 planes appear as black and white bands and are easily resolved. The 110 planes are harder to identify and run perpendicular to the 002 planes (point A in Fig. 12). The TEM observations support the supposition that the graphite crystals within the foam ligaments are highly aligned and will exhibit an extremely large thermal conductivity.

Examination of the junction region (Fig. 13), shows that the graphene basal planes are continuous around the fold and that there are bifurcations in the fold region (region A). Curiously, there is not a continuous line where the fold occurs, instead there is a general region where the planes shift direction. A fold is formed when two mesophase crystals touch and the graphene layers are unable to align properly. The graphitic planes in the fold region likely contain defects, resulting in the curvature around the fold. Due to these defects, the junctions may act more like a polycrystalline graphite compared to the ligaments.

Based on our observations of foam structure, the highest thermal conductivity is expected in the foam ligaments where the graphite structure is most perfect. The thermal conductivity should be greater than that of mesophase fibers but less than that of perfect graphite. The junction regions, while exhibiting alignment of the graphite planes, contain defects and folds, reducing the thermal conductivity.

4.4. X-ray diffraction

Microscopy studies offer purely qualitative data regarding the aligment of the graphite crystals in the ligaments and the junctions, while X-ray diffraction can give quantitative data. X-ray data, however, need to be treated with extreme caution. Fig. 14 shows diffraction patterns for three graphite foams with different densities. Initial inspection shows no discernable differences in the crystalline nature of the foam. However, further analysis of the patterns to calculate the crystal parameters reveals that density does affect the stacking height,

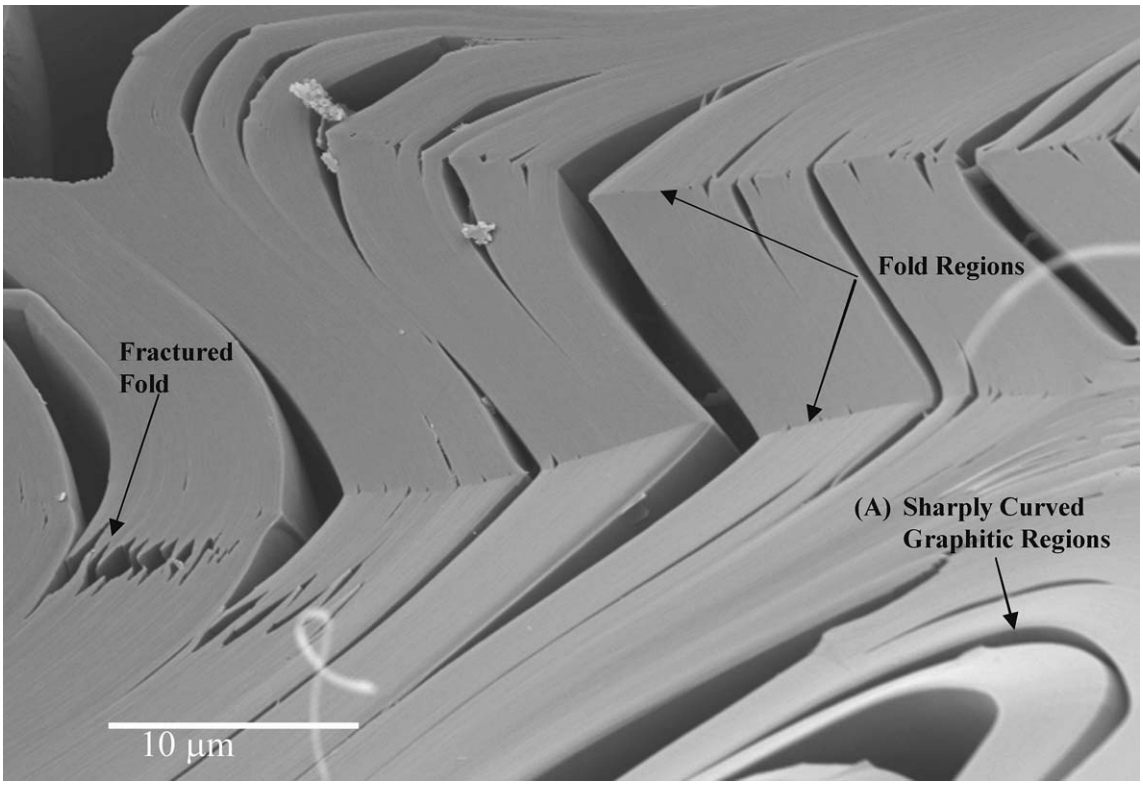

Figure 11 SEM image of graphite foam B graphitized at 1°C/min illustrating folding of graphitic planes within the junction regions.

L_c, but not interlayer spacing, d_{002}, or coherence length, L_a (Table III). This result is expected since a change in foam density changes the thickness of the ligaments, resulting in larger stacking of the crystals. Ruland [67–69] suggests that curvatures in large graphite crystals can affect the length of the coherent stacking by disrupting the ABA structure. The X-ray beam is diffracted at what would appear to be a lattice defect but, in reality, is a shift in the ABA positions. If this is the case, the curvatures of the crystals found in the ligaments would be measured as a series of short straight sections in the ligaments to yield an "apparent" coherence length which would not be dependent on density. This potentially explains why the stacking height of the foam is more than an order of magnitude greater than the coherence length which is atypical of highly ordered graphites.

Fig. 15 plots the interlayer *d*-spacing of the graphitic materials reported in Table III. As clearly evident, the thermal conductivity (parallel to the graphitic planes) of the materials increase significantly with lowering *d*-spacing. If we plot the average *d*-spacing for the foam ligaments on this graph (dashed line), we can estimate that the average thermal conductivity of the ligaments should range from about 1300–1700 W/m·K. So, a conservative estimate for the average thermal conductivity of the foam ligaments would be 1300 W/m·K.

5. Model development and analysis

There have been several models proposed for heat transfer with porous materials [72–82]. Some of these also include a model for the thermal properties of bulk foams, typically relating the ligament properties to the

TABLE III Measured crystallographic parameters of the graphitic foams along with measured data of graphitic fibers found in literature

Material	Density (g/cm^3)	Ligament density (g/cm^3)	d_{002} (nm)	$L_{c,002}$ (nm)	$L_{a,110}$ (nm)	Thermal conductivity (W/m·K)
Graphite foam ligaments[b]	0.29	2.23[a]	0.3356	152	28	?
Graphite foam ligaments[b]	0.51	2.23[a]	0.3356	208	29	?
Graphite foam ligaments[b]	0.64	2.23[a]	0.3356	437	28	?
E120 [70]	2.20	2.20	0.3409	18.9	51.4	265
E130 [70]	2.20	2.20	0.3380	24.0	180	525
E1 [55]	–	–	0.3364	102	–	1060
E2 [55]	–	–	0.3368	41.5	–	746
P1 [55]	–	–	0.3368	71	–	862
P2 [55]	–	–	0.3372	77	–	661
K1100 Fiber [55]	–	–	0.3366	51	85	884
VGCF [71]	–	–	0.335	100	–	1950
ThermalGraph® [55]	–	–	0.3364	99	–	991

[a]Measured with helium pycnometry.
[b]Graphite foam B, 10°C/min.

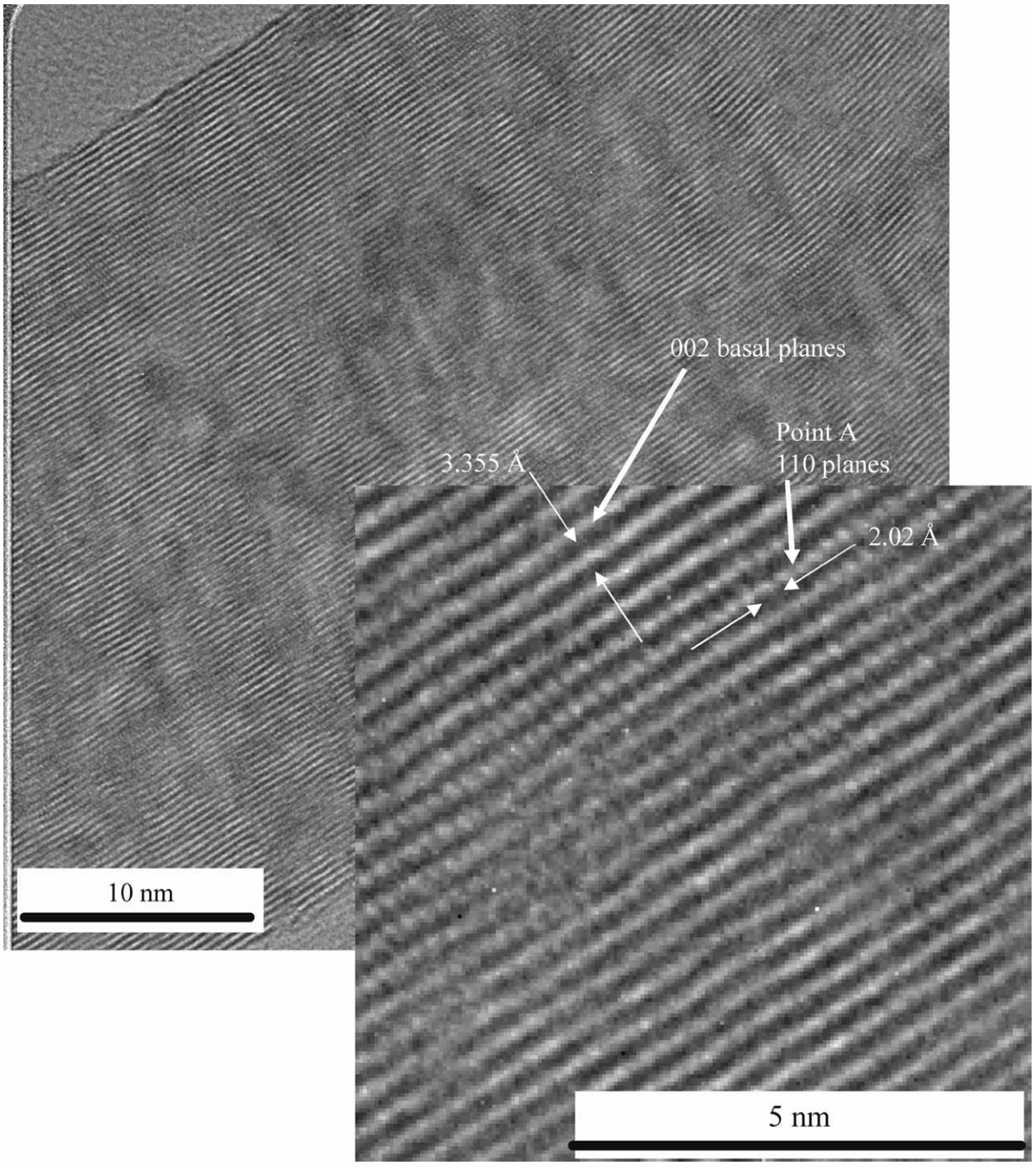

Figure 12 TEM images of graphite foam ligament illustrating highly ordered nature of the structure.

relative density in some fashion (see Equation 1 [83] and 2, [84]). The models for foam conductivity can be much more complicated (see Equation 3 [85]), but will not be explaind here for simplicity.

$$\lambda_{\text{bulk}} = 0.35\left(\frac{\rho_{\text{bulk}}}{\rho_{\text{solid}}}\right)\lambda_{\text{solid}}, \tag{1}$$

where λ_{bulk} is the bulk thermal conductivity, ρ_{bulk} is the bulk density, ρ_{solid} is the skeletal density, and λ_{solid} is the average thermal conductivity of the ligaments.

$$\lambda_{\text{solid}}\left(\frac{\rho_{\text{bulk}}}{\rho_{\text{solid}}}\right)^{1.8} < \lambda_{\text{bulk}} < \lambda_{\text{solid}}\left(\frac{\rho_{\text{bulk}}}{\rho_{\text{solid}}}\right)^{1.6}, \tag{2}$$

$$\bar{\lambda} = \frac{1}{4\pi}\int_0^{\pi}\int_0^{2\pi} \lambda^* n(\theta, \psi)\sin\theta \mathrm{d}\psi \mathrm{d}\theta, \tag{3}$$

where $\bar{\lambda}$ is the bulk conductivity, λ^* is the average ligament conductivity, and n is the unit normal director for the ligament.

Assuming a conservative average ligament conductivity of 1300 W/m·K, predicted bulk thermal conductivities (using Equations 1 and 2) are compared to the measured data [39] in Fig. 16. Equation 1 predicts a linear response of thermal conductivity versus density. In this equation, the coefficient 0.35 is, in effect, a factor which accounts for the tortuosity of the heat flow path length. According to Fourier's Law of Heat Conduction, the effective heat transfer is related to the inverse in the path length. Since this path length is around a sphere, (path length of about pi), the inverse is approximately 0.35. This equation was developed for sintered metal porous media used in heat pipes [83]. Unfortunately, this is essentially solid particulates

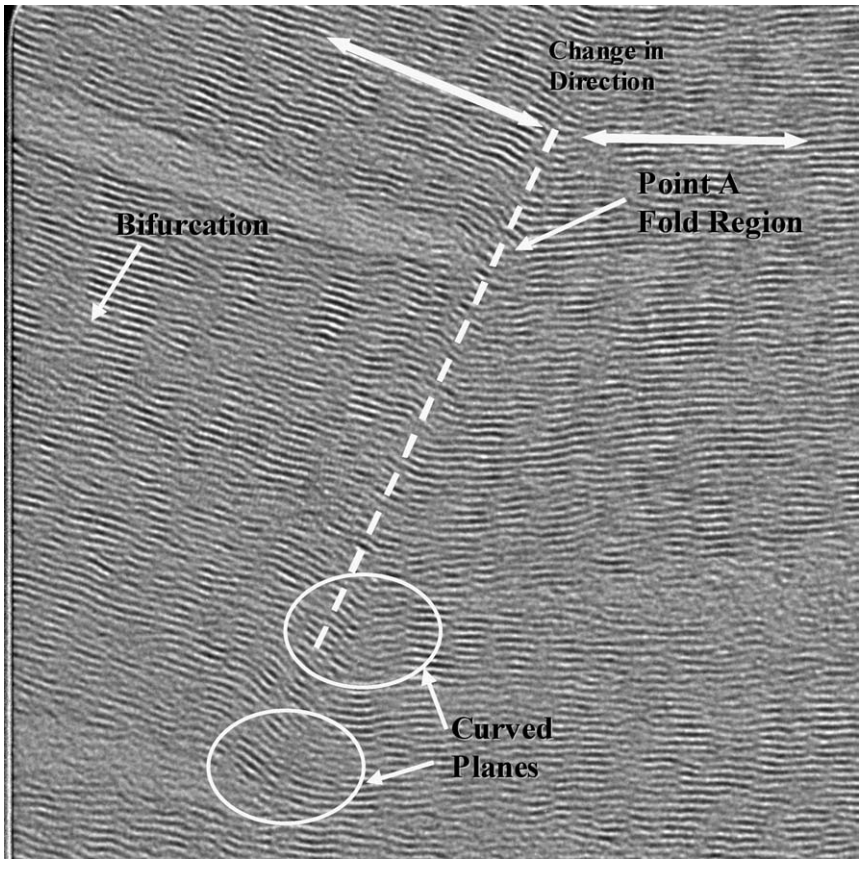

Figure 13 High magnification TEM image of a fold region in a junction of ORNL graphite foam.

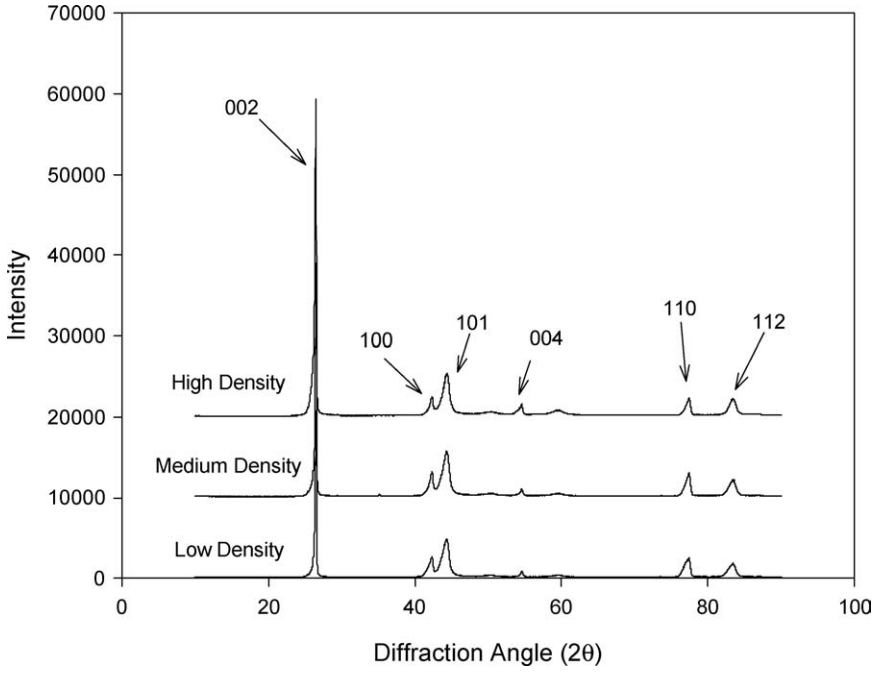

Figure 14 X-ray diffraction patterns of several graphite foams indicating highly graphitic strucuture.

joined at the contact points, rather than a foam, and Equation 1 under predicts the thermal conductivity for foams.

Equation 2 predicts a range of thermal conductivities with an exponential relationship to density. This model was reported by Haack of Porvair Fuel Cell, Inc. for reticulated metal foams with hollow ligaments (similar in structure to Fig. 16a). Although this relationship works well at the higher densities, it under predicts the thermal conductivity at the lower densities for the graphite foam. In this equation, the exponent is a factor expressing the effects of the ratio of the volume of ligament junctions to the volume of ligaments. In other words, as the ligament junctions become larger, there may be more impedance in the heat transfer, reducing conductivity.

Both Equations 1 and 2 seem to be based on assumptions that do not fit the unique structure of the

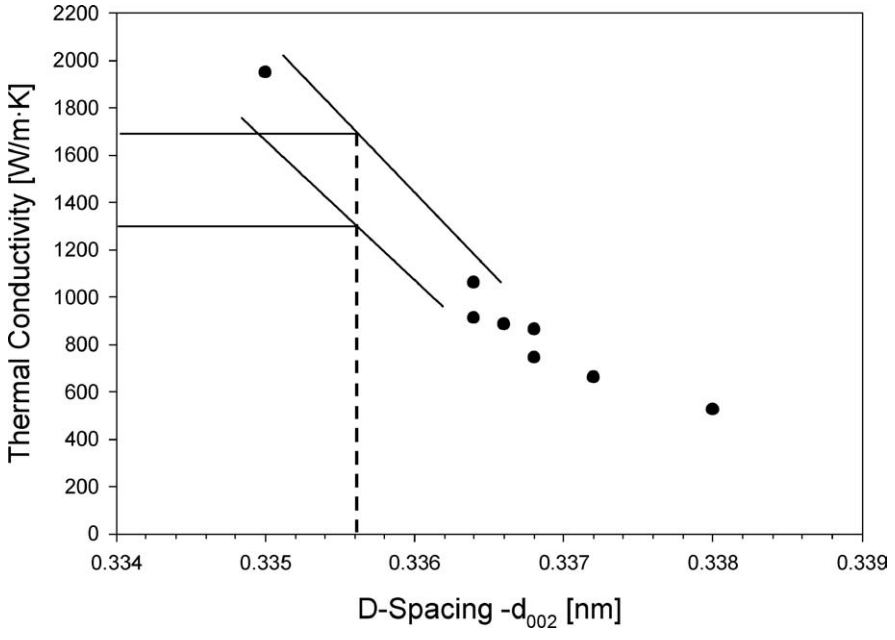

Figure 15 Plot of thermal conductivity parallel to the graphite plane in various graphitic materials versus interlayer *d*-spacing.

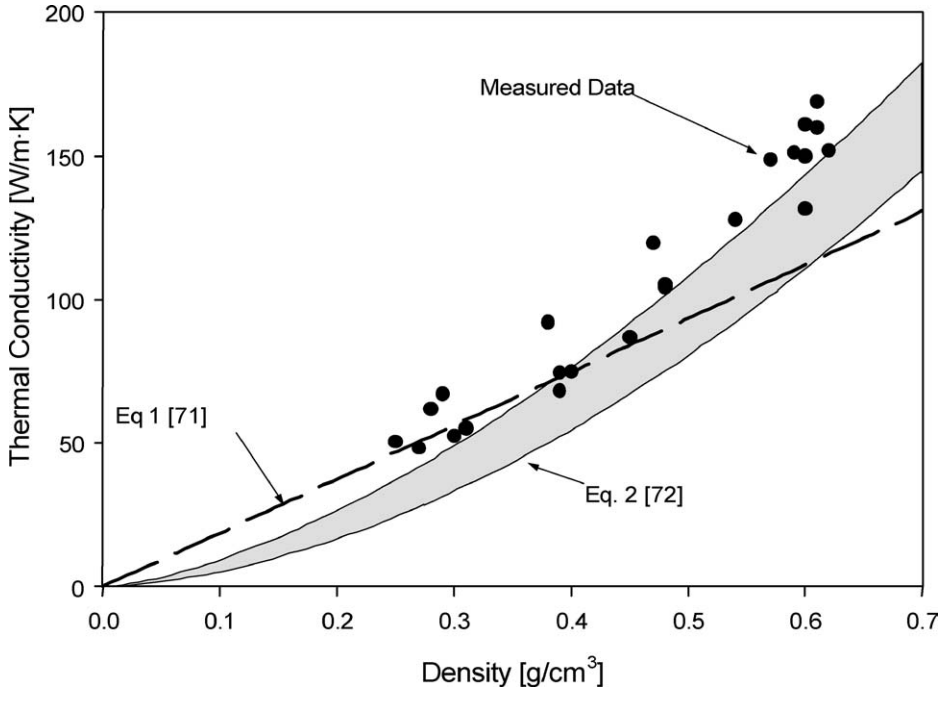

Figure 16 Measured thermal conductivities of ORNL graphite foam compared to typical models for thermal conductivities of foams using an estimated ligament conductivity of 1300 W/m·K.

graphite foams and the need for improved model is indicated.

There are three main features that should be included to model the thermal conductivity of the foam: (1) ligament conductivity, (2) relative density, and (3) heat flow path length. First, the ligament conductivity is linearly related to the bulk conductivity (as in both Equations 1 and 2). Next, as relative density increases the conductivity increases for two reasons: (1) simply an increase in mass for heat transfer, and (2) change in the ratio of junction material to ligament material (which we have shown can be drastically different in relative structural order). For example, in a foam that is reticulated (Fig. 17a), the relative volume fraction of junctions to ligaments will be much smaller than that in a foam with a spherical cell structure (Fig. 17b or c). As the foam increases in density, the ratio of junction to ligaments (which are more like cell walls) will increase, so the effect of relative density will be different in each of these cases. Last, the heat flow path length (which is an essential element in the Fourier equation for heat transfer) is critical. Simply, the heat must follow a path around the sphere, rather than through a linear path as in a solid material. This coefficient is independent of average conductivity of the ligaments, and is directly related to the pore cellular structure. For example, graphite foams (Fig. 17b) that have been heat treated to different graphitization temperatures, would have drastically

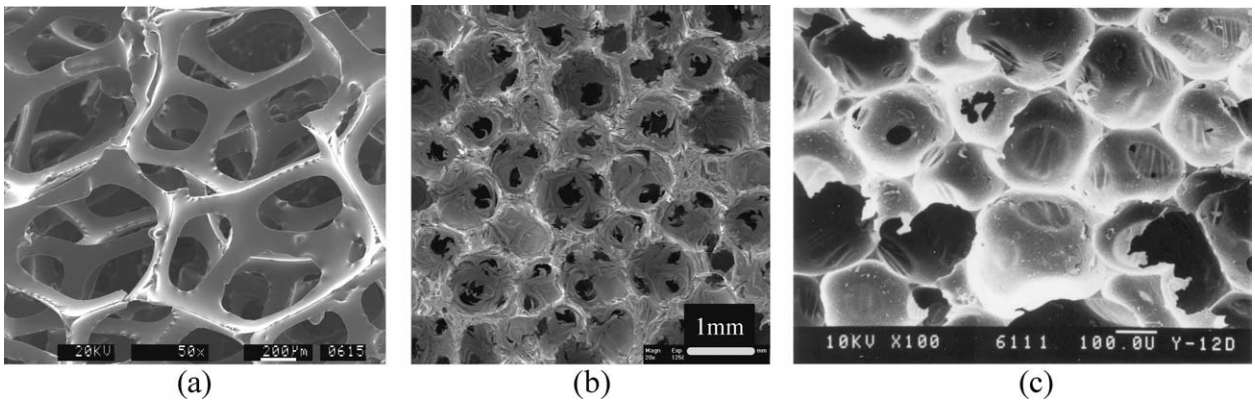

Figure 17 SEM micrographs of (a) reticulated carbon foam (Duocel^{TM} [64]), (b) mesophase carbon foams (ORNL), and (c) urethane derived closed cell carbon foams.

ligament conductivities in the equation, but exactly the same structural coefficients. Hence, this coefficient cannot be linked with the ligament conductivity coefficient. This is because it is desired to determine an equation in which different ligament conductivities can be applied based on different relative graphitization temperatures of the material.

Unlike metallic or glassy foams, foams made from graphite contain material that is locally anisotropic and orientation of the graphite basal planes parallel to the heat flow is critical. Keep in mind that the theoretical thermal conductivity of perfect graphite along crystallographic basal planes is more than 2000 W/m·K at room temperature, but less than 10 W/m·K perpendicular the basal planes [46]. Therefore, in regions with poor crystallographic alignment, such as at the junctions, the local thermal conductivity will be lower than that in the ligaments. Such regions will significantly affect the thermal conductivity of the bulk foam. Therefore, simple models, such as Equations 1 and 2, are not representative of the thermal properties in the graphite foam. It is proposed that the following equation is more reasonable for the graphitic foams.

$$\lambda_{\text{bulk}} = \alpha \left(\frac{\rho_{\text{bulk}}}{\rho_{\text{solid}}} \right)^{\text{m}} \lambda_{\text{solid}} \tag{4}$$

where, α = cellular structural coefficient—factor incorporating the effect of pore shape on the inverse in heat flow length path, m = factor incorporating effect of density on volume ratio of ligament to junctions and the result on increased heat flow path, ρ_{bulk} = bulk density (g/cm^3), ρ_{solid} = density of ligaments (g/cm^3), and λ_{solid} = average thermal conductivity of ligaments and junction.

This model attempts to account for the three key aspects of thermal conductivity previously discussed. The constants α and m are functions of the pore structure and are determined from measured thermal properties of the foams by regression techniques. It is again noted here that the average ligament conductivity and cellular structural coefficient (α) can be linked into one coefficient to perform the least squares analysis of existing data. However, the resulting curve fit will only be applicable to foams which have been process in exactly the same manner. Hence, to apply the equation to other mesophase pitch derived graphite foams, an assumed ligament conductivity for the curve fit coefficient will be factored out to calculate α for the class of foams.

From the previous discussions in Section 3, it is evident that the junctions of the graphite foam are highly graphitic, but more randomly oriented and cracked than the ligaments which exhibit an extremely aligned structure. These results indicate that the assumptions that the previous equations which used a uniform material property are not appropriate to the graphite foam. Hence, it makes sense that in the graphite foams, the microstructure in the ligaments and junctions will combine to form an average material property. However, we have also shown that the relative ratio between the volume fraction of the ligaments to the junctions will play a role in affecting the heat flow paths, which is separate from the average material conductivity. Therefore, by fitting Equation 4 to the data in Fig. 4, we obtained the following constants:

$$\alpha\lambda_{\text{solid}} = 954.4,$$
$$m = 1.427.$$

Applying the conservative estimate for ligament conductivity from previous discussions in Section 4.4 of about 1300 W/m·K, the coefficients reduce to

$$\alpha = 0.734,$$
$$m = 1.427,$$
$$\lambda_{\text{solid}} = 1300 \text{ W/m·K}.$$

thus,

$$\lambda_{\text{bulk}} = 0.734 \left(\frac{\rho_{\text{bulk}}}{\rho_{\text{solid}}} \right)^{1.427} (1300).$$

The resulting relationship is plotted in Fig. 18.

This model, for the 10°C/min heat treated material, may under-predict the thermal conductivity of the foam heat treated at 1°C/min. Hence if we apply the equation to foam fabricated with a slower heat treatment, we can estimate the average ligament conductivity for this foam. By using the data of Table I for ORNL graphite foam B graphitized at 1°C/min, (rather than 10°C/min

TABLE IV Results of model

	Relative density (%)	Estimated average ligament conductivity (W/m·K)	Measured apparent bulk conductivity (W/m·K)	Predicted apparent bulk conductivity (W/m·K)
ORNL graphite foam[a]	26.5	1300	150	149
ORNL graphite foam[b]	26.5	1640	181	181
PocoFoam™	27	1640	182	186

[a]Graphitized at 10°C/min.
[b]Graphitized at 1°C/min.

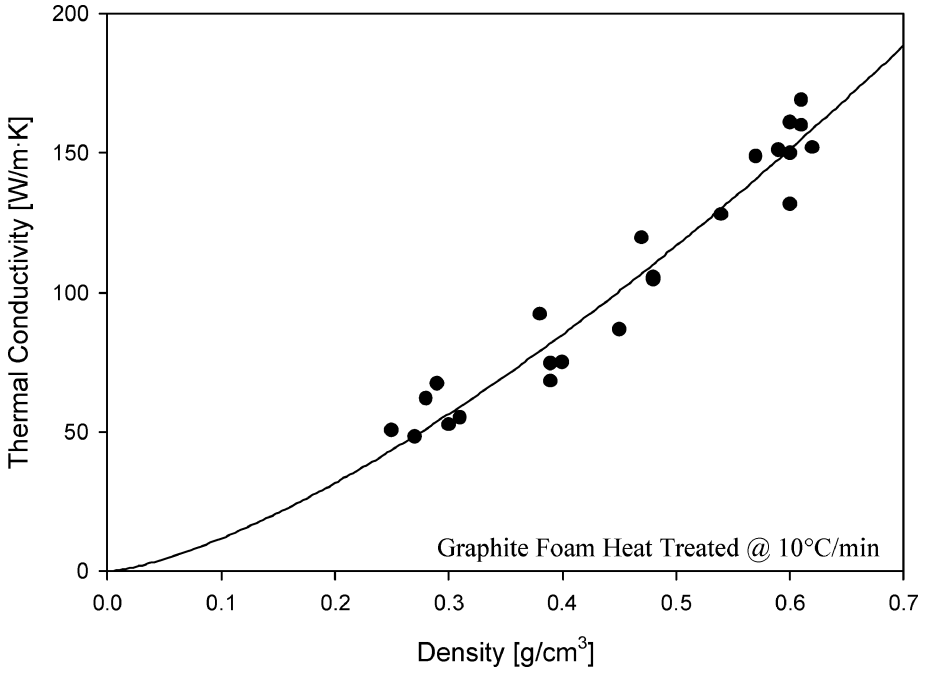

Figure 18 Plot of measured data and results of a new model which incorporates (1) ligament conductivity, (2) relative density, and (3) heat flow path length.

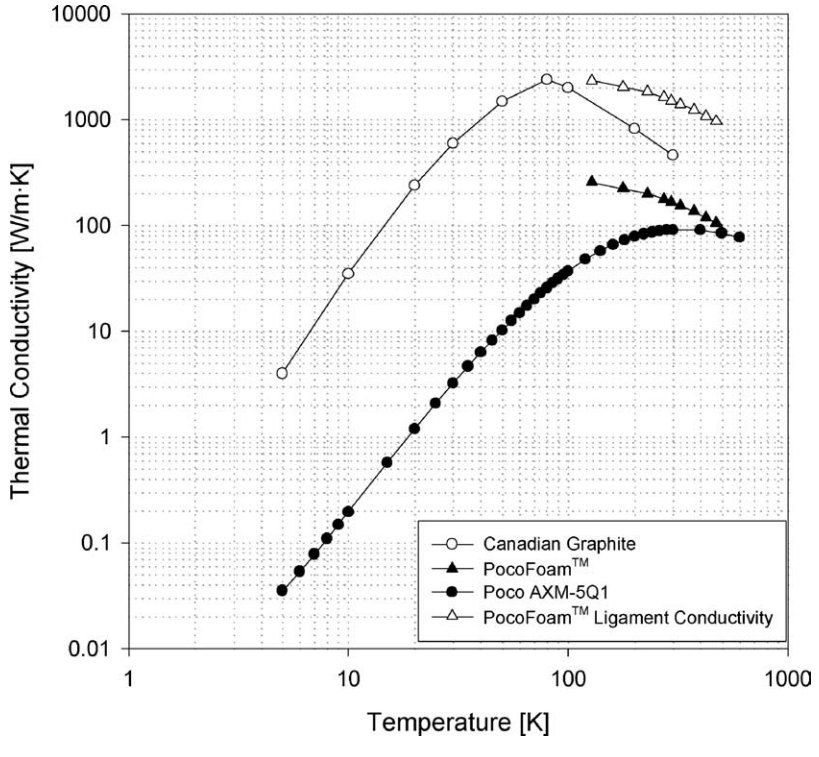

Figure 19 Plot of estimated ligament conductivity of PocoFoam™ versus other graphites illustrating nearly perfect graphite behavior at low temperatures.

used to curve fit the equation), we calculate an average ligament conductivity of 1640 W/m·K. This is anticipated as the foam with the slower heat treatment has a better crystal properties (d_{002}, L_c, and L_a) corresponding to a higher average ligament conductivity. Applying these values to the PocoFoam®, which is assumed to be processed with similar conditions to the ORNL Foam B-1°C/min, we estimate that the bulk conductivity should be 186 W/m·K, versus the measured 182 W/m·K.

If these constants are then used to calculate the average ligament properties of the PocoFoam™ at cryogenic temperatures, illustrated in Fig. 3, the results are remarkable and shown Fig. 19. In fact, the ligaments of the foam appear to exhibit a maximum temperature similar to that of the Canadian natural graphite, clearly indicating that the foam consists of highly ordered graphitic structures approaching that of perfect graphite. Again, note that these estimated values are based on the assumption that the structural coefficient value does not change with change in heat treatment rate, only foam processing conditions, and therefore, the structural coefficient can be separated from the average ligament conductivities in the equation. In addition, it is also noted that the average ligament conductivities are an average between the junctions and ligaments, and thus it is assumed that the actual ligaments with high order have a higher conductivity than the estimated average ligament property used in the equation. What is of significance is that the average ligament properties are in the "ball park" of that with highly ordered natural graphite.

6. Conclusions

Optical microscopy, scanning electron microscopy, transmission electron microcsopy, X-ray diffraction, and thermal analysis have shown that the graphite foam exhibits a structure unlike most other synthetic graphite materials. In fact, the thermal properties of the foam ligaments are similar to natural Canadian graphite (commonly assumed to be the most highly aligned of the natural graphites) and approaching that of highly orderd pyrolytic graphite (HOPG). The estimated ligament conductivities are extremely high, although the junctions are not as thermally conductive yet still highly graphitic. Simple models of heat transfer through the foam do not take into account this difference, so a weighted average value between the junctions and the ligaments is assumed for foam models (in the neighborhood of 1640 W/m·K).

Based upon both qualitative and quantative analyses, variables for a new model were made for foams fabricated at a final heat treatment rate of 10°C/min. SEM and TEM studies showed that there were fewer microcracks and better alignment of the crystals in the junctions for foams made at a heat treatment rate of 1°C/min. Hence, it was assumed that the average ligament conductivities should be higher for the material heat treated at 1°C/min compared to that heat treated at 10°C/min. The average ligament conductivity for the higher performance foam was estimated at 1650 W/m·K, significantly higher than the best mesophase based graphite fibers. The correlations result from fitting existing data, and should only be applied to foams made with similar processing parameters. Process changes may result in foams with a similar macrostructure, but a significantly different microstructure in the ligaments and junctions.

The modeling results suggest that modifying the junctions likely is crucial to improve the thermal properties of the material. Therefore, process changes that only affect the structure slightly, such as heat treatments, will not necessarily have a large impact on the thermal properties. Process changes that modify the pitch precursor to produce a junction which is less cracked and more ordered offers great potential to improve the properties of the foams.

Acknowledgements

The authors wish to thank Karen More of Oak Ridge National Laboratory for her excellent work in transmission electron microscopy and interpretation of the results. In addition, the authors wish to thank Tom Geer for performing the preparation of the samples for optical image analysis.

This research was sponsored by the U.S. Department of Energy, Assistant Secretary for Energy Efficiency and Renewable Energy, Office of Freedom Car and Vehicle Technologies, as part of the Automotive Propulsion Materials Program, under contract DE-AC05-00OR22725 with UT-Battelle, LLC.

"The submitted manuscript has been authored by a contractor of the U.S. Government under contract No. DE-AC05-00OR22725. Accordingly, the U.S. Government retains a nonexclusive, royalty-free license to publish or reproduce the published form of this contribution, or allow others to do so, for U.S. Government purposes."

References

1. W. FORD, Method of Making Cellular Refractory Thermal Insulating Material, US Patent 3,121,050, 1964.
2. J. GOOGIN, J. NAPIER and M. SCRIVNER, Method for Manufacturing Foam Carbon Products, US Patent 3,345,440, 1967.
3. F. C. COWLARD and J. C. LEWIS, *J. Mater. Sci.* **2** (1967) 507.
4. W. F. KNIPPENBERG and B. LERSMACHER, *Phillips Techn. Rev.* **36** (1976) 93.
5. T. NODA, M. INAGAKI and S. YAMADA, *J. Non-Cryst. Solids* **1** (1969) 285.
6. R. D. KLETT, High Temperature Insulating Carbonaceous Material, US Patent 3,914,392, 1975.
7. A. BONZOM, A. P. CREPAUX and A.-M. E. J. MONTARD, Process for Preparing Pitch Foams and Products so Produced, US Patent 4,276,246, 1981.
8. B. ETTINGER and S. WOLOSIN, Refractory Porous Bodies, US Patent 3,666,526, 1972.
9. H. LUHLEICH *et al*., Method of Making Carbonaceous Bodies, US Patent 3,927,187, 1975.
10. R. MAREK and W. UDICHAK, Foam Carbonization and Resulting Structure, US Patent 3,922,334, 1975.
11. H.-G. FRANCK *et al.*, Process for Making a Foam from a Composition Comprising Bituminous Masses, a Novolac, and Hexamethylenetetramine, US Patent 3,784,487, 1974.
12. C. VINTON and C. FRANKLIN, Method for the Preparation of Carbon Structures, US Patent 3,927,186, 1975.
13. J. W. HAGER, *Mater. Res. Soc. Symp. Proc.* **270** (1992) 41.
14. J. W. HAGER and D. P. ANDERSON, 21st Biennial Conference on Carbon Extended Abstracts, 1993, p. 102.

15. *Idem.*, 40th International Sampe Symposium, Anaheim, California, May 8–11, 1995.
16. J. W. HAGER and M. L. LAKE, *Mater. Res. Soc. Symp. Proc.* **270** (1992) 29 .
17. J. W. HAGER, J. W. NEWMAN, N. JOHANNES and F. H. TURRILL, Carbon Artifacts and Compositions and Processes for Their Manufacture, US Patent 6,013,371, 2000.
18. S. S. SANDHU and J. W. HAGER, *Mater. Res. Soc. Symp. Proc.* **270** (1992) 35.
19. K. KEARNS, 21st Annual Conference on Composites, Materials, and Structures, Cocoa Beach, Florida, January 26–31, 1997, p. 835.
20. K. M. KEARNS, Process for Preparing Pitch Foams, US Patent 5,868,974, 1999.
21. A. H. STILLER, P. G. STANSBERRY and J. W. ZONDLO, Method of Making a Carbon Foam Material and Resultant Product, US Patent 5,888,469, 1999.
22. A. H. STILLER, A. YOCUM and J. PLUCINSKI, Method of Making a Reinfoced Carbon Foam Material and Related Product, US Patent 6,183,854, 1999.
23. A. H. STILLER, P. STANSBERY and J. ZONDLO, Method of Making a Carbon Foam Material and Resultant Product, US Patent 6,346,226, 2001.
24. *Idem*., Method of Making a Carbon Foam Material and Resultant Product, US Patent 6,241,957, 1999.
25. J. KLETT, in Proceedings of the 1998 43rd International SAMPE Symposium and Exhibition, Part 1 (of 2), Anaheim, California, U.S.A., May 31–June 4, 1998, p. 745.
26. *Idem*., *J. Comp. Manufact.* **15** (1999) 1.
27. *Idem*., Process for Making Carbon Foam, US Patent 6,033,506, 2000.
28. *Idem*., Pitch-Based Carbon Foam and Composites, US Patent 6,261,485, 2001.
29. *Idem*., Pitch Based Foam with Particulate, US Patent 6,287,375, 2001.
30. *Idem*., Method for Extruding Pitch Based Foam, US Patent 6,344,159, 2002.
31. *Idem*., Pitch Based Carbon Foam and Composites, US Patent 6,387,343, 2002.
32. *Idem*., Method of Casting Pitch Based Foam, US Patent 6,398,994, 2002.
33. J. KLETT and T. BURCHELL, Pitch Based Carbon Foam Heat Sink with Phase Change Material, US Patent 6,399,149, 2002.
34. J. KLETT and T. D. BURCHELL, Science and Technology of Carbon, Strasbourg, France, July 8–9, 1998.
35. J. KLETT, C. WALLS and T. D. BURCHELL, Carbon '99, Charleston, SC, July 11–16, 1999.
36. J. W. KLETT, A. McMILLAN and N. GALLEGO, "Carbon Foam for Electronics Cooling" (National Laboratory Fuel Cell Annual Report, FY, 2002).
37. D. D. EDIE and M. G. DUNHAM, *Carbon* **27** (1989) 647 .
38. J. L. WHITE and P. M. SHEAFFER, *ibid.* **27** (1989) 697.
39. J. KLETT, R. HARDY, E. ROMINE, C. WALLS and T. BURCHELL, *ibid.* **38** (2000) 953.
40. R. D. COWAN, *J. Appl. Phys.* **34** (1962) 926.
41. ASTM, "Annual Book of ASTM Standards" (1999) Vol. C714.
42. ASTM, *ibid.* (1999) Vol. C781.
43. T. M. BESMANN, B. W. SHELDON, R. A. LOWDEN and D. P. STINTON, *Science* **253** (1991) 1104 .
44. K. L. MORE, D. W. COFFEY, B. A. PINT, K. S. TRENT and P. F. TORTORELLI, in Proceedings of Microscopy & Microanalysis, 2000, p. 540.
45. H. KLUG and LEALEXANDER, in "X-Ray Diffraction Procedures for Polycrystalline and Amorphous Materials" 2nd ed. (J. Wiley, New York, USA, 1974).
46. B. T. KELLY, "Physics of Graphite" (Applied Science Publishers, London, 1981).
47. *Idem.*, *Carbon* **6** (1968) 485.
48. *Idem.*, *ibid.* **6** (1968) 71 .
49. *Idem.*, *ibid.* **5** (1967) 247 .
50. *Idem.*, in "Chemistry and Physics of Carbon," edited by P. L. Walker Jr. and P. A. Thrower (Marcell Dekker, Incorporated, New York) Vol. 10, p. 1.
51. *Idem.*, in "Chemistry and Physics of Carbon," edited by P. L. Walker Jr. and P. A. Thrower (Marcell Dekker, Incorporated, New York, 1968) Vol. 10, p. 1.
52. *Idem.*, *Phys. Chem. Carbon* **5** (1969) 119.
53. P. G. KLEMENS, *Aust. J. Appl. Phys.* **6** (1953) 405 .
54. *Idem.*, in "Solid State Physics," edited by F. Seitz and D. Turnbull (Academic Press, Inc., New York, 1958) p. 1.
55. P. M. ADAMS, H. A. KATZMAN, G. S. RELLICK and G. W. STUPIAN, *Carbon* **36** (1998) 233.
56. R. C. LINCOLN and R. C. HECKMAN, *High Temperatures—High Pressures* **7** (1975) 71.
57. C. N. HOOKER, A. R. UBBELOHDE, F. R. S. YOUNG and D. A. YOUNG, *Proc. Royal Soc.* A **276** (1963) 83.
58. C. P. JAMIESON and S. MROZOWSKI, The Conference on Carbon, 1956, p. 155.
59. C. A. KLEIN and M. P. LEPIE, *Solid State Electr.* **7** (1964) 241.
60. A. R. UBBELOHDE and F. R. S., J. ORR, *Nature* **179** (1957) 193.
61. J. G. HUST, "A Fine-Grained, Isotropic Graphite for Use as NBS Thermophysical Property RM's from 5 to 2500K" Tech. Report No. 260-89 (National Bureau of Standards, 1984).
62. A. W. SMITH and N. S. RASOR, *Phys. Rev.* B **104** (1956) 885.
63. P. DEBYE, *Annalen der Physik* **39** (1912).
64. "ERG Product Literature" (2000).
65. "Porvair Product Literature" (2000).
66. J. E. ZIMMER and J. L. WHITE, "Advances in Liquid Crystals" (Academic Press, Inc., 1982) Vol. 5.
67. W. RULAND, *Acta Cryst.* **18** (1965) 992.
68. *Idem.*, in "Chemistry and Physics of Carbon," edited by P. L. Walker Jr. (Marcel Dekker, INC., New York, 1968) Vol. 4, p. 1.
69. W. RULAND and H. TOMPA, *Acta Cryst.* A **24** (1968) 93.
70. B. NYSTEN, J.-P. ISSI, R. BARTON JR., D. R. BOYINGTON and J. G. LAVIN, *Phys. Rev.* B **44** (1991) 2142 .
71. J. HEREMANS, R. I. and M. S. DRESSELHAUS, *ibid.* **32** (1985) 6742.
72. K. BOOMSMA and D. POULIKAKOS, *J. Heat Mass Transfer* **44** (2001) 827.
73. V. V. CALMIDI and R. L. MAHAJAN, *ASME J. Heat Transfer* **121** (1999) 466.
74. *Idem.*, *ibid.* **122** (2000) 557.
75. M. L. HUNT and C. L. TIEN, *Int. J. Heat Mass Transfer* **31** (1988) 301.
76. S. B. SATHE, B. G. SAMMAKIA, A. C. WONG and H. V. MAHANEY, National Heat Transfer Conference, 1995, p. 43.
77. D. ANGRIASA and G. P. PETERSON, *J. Electr. Pack.* **121** (1999) 1.
78. D. ANGRIASA, *Intern. J. Heat Mass Transfer* **45** (2001) 919.
79. B. V. ANTOHE, J. L. LAGE, D. C. PRICE and R. M. WEBER, *Trans. ASME* **119** (1997) 404.
80. *Idem.*, *Intern. J. Heat Fluid Flow* **17** (1996) 594.
81. A. BHATTACHARYA, V. V. CALMIDI and R. L. MAHAJAN, *Intern. J. Heat Mass Transfer* **45** (2002) 1017.
82. A. BHATTACHARYA and R. MAHAJAN, 34th National Heat Transfer Conference, Pittsburg, PA, 2000.
83. M. NORTH, DARPA Workshop on Porous Metals, Crystal City, VA, 1997.
84. D. HAACK, D. BUTCHER, T. KIM and T. J. LU, "Novel Lightweight Metal Foam Heat Exchangers" (Porvair Fuel Cells, 2001).
85. C. C. TEE, J. W. KLETT, D. P. STINTON and N. YU, in Proceedings of the 24th Bienial Conference on Carbon, Charleston, SC, USA, 1999, p. 130.

Received 28 May 2003
and accepted 3 February 2004